

Experimental Validation of Pulse Phase Tracking for X-ray Pulsar Based Spacecraft Navigation

Kevin Anderson

November 27, 2012

Scholarly Paper submitted to the Faculty of the Graduate School of the University of Maryland, College Park, in
partial fulfillment of the requirements for the degree of Master of Science in Aerospace Engineering

Scholarly Paper Committee:
Dr. Darryll J. Pines (Advisor)
Dr. Derek Paley

Abstract

Pulsars are a form of variable celestial source that have shown to be usable as aids for autonomous, deep space navigation. Particular those sources emitting in the X-ray band are ideal for navigation due to smaller detector sizes. In this paper X-ray photons arriving from a pulsar are modeled as a non-homogeneous Poisson process. The method of pulse phase tracking is then investigated as a technique to measure the radial distance traveled by a spacecraft over an observation interval. A maximum-likelihood phase estimator (MLE) is used for the case where the observed frequency signal is constant. For the varying signal frequency case, an algorithm is used in which the observation window is broken up into smaller blocks over which an MLE is used. The outputs of this phase estimation process were then looped through a digital phase-locked loop (DPLL) in order to reduce the errors and produce estimates of the doppler frequency. These phase tracking algorithms were tested both in a computer simulation environment and using the NASA Goddard Spaceflight Center X-ray Navigation Laboratory Testbed (GXLT). This provided an experimental validation with photons being emitted by a modulated X-ray source and detected by a silicon-drift detector. Models of the Crab pulsar and the pulsar B1821-24 were used in order to generate test scenarios. Three different simulated detector trajectories were used to be tracked by the phase tracking algorithm: a stationary case, one with constant velocity, and one with constant acceleration. All three were performed in one-dimension along the line of sight to the pulsar. The first two had a constant signal frequency and the third had a time varying frequency. All of the constant frequency cases were processed using the MLE, and it was shown that they tracked the initial phase within 0.15% for the simulations and 2.5% in the experiments, based on an average of ten runs. The MLE-DPLL cascade version of the phase tracking algorithm was used in the varying frequency case. This resulted in tracking of the phase and frequency by the DPLL outputs in both the simulation and experimental environments. The crab pulsar was experimentally tested with a trajectory with a higher acceleration. In this case the phase error tended toward zero as the observation extended to 250 seconds and the doppler frequency error tended to zero in under 100 seconds.

Contents

Abstract	2
List of Nomenclature	4
List of Figures	5
List of Tables	5
1 Introduction	6
1.1 Background	6
1.2 Suggested Approach	7
2 X-Ray Pulsar Signal Model	8
2.1 Non-Homogeneous Poisson Process	8
2.2 Pulsar Rate Function	8
2.2.1 Constant Observed Signal Frequency	9
2.2.2 Time-Varying Observed Signal Frequency	10
3 Maximum-Likelihood Initial Phase and Frequency Estimation	10
4 Pulse Phase Tracking	11
4.1 Digital Phase-Locked Loops	11
5 Simulation Structure	12
6 Experimental Procedure	13
7 Results and Discussion	15
7.1 Simulation Results	15
7.2 Experimental Results	18
8 Conclusion	22
Acknowledgements	23
References	24

Nomenclature

Terminology

Delta-DOR	Differential One-Way Ranging
DPLL	Digital Phase-Locked Loop
GSFC	Goddard Space Flight Center
GXLT	GSFC X-ray Navigation Laboratory Testbed
ISS	International Space Station
LED	Light Emitting Diode
LLF	Logarithm of the Likelihood Function
MLE	Maximum-Likelihood Estimator
MSP	Millisecond Period Pulsar
MXS	Modulated X-Ray Source
NASA	National Aeronautics and Space Administration
NCO	Numerically Controlled Oscillator
NICER	Neutron Star Interior Composition ExploreR
NHPP	Non-Homogeneous Poisson Process
PDF	Probability Density Function
SDD	Silicon Drift Detector
SEXTANT	Station Explorer for X-ray Timing and Navigation Technology
SNR	Signal to Noise Ratio
SSB	Solar System Barycenter
TOA	Time of Arrival
UV	Ultraviolet
VLBI	Very Long Baseline Interferometry
XDET	Time-Tagging X-Ray Detector
XDPG	X-Ray Digital Pulse Generator
XNAV	X-ray Pulsar-Based Navigation

Symbols

α	Effective Source Photon Arrival Rate (photons/second)
β	Effective Background Photon Arrival Rate (photons/second)
$\lambda(t)$	Pulsar NHPP Rate Function
ϕ	Phase
ϕ_{det}	Observed Phase at the Detector
ρ	Pulse Fraction (Ratio of Pulsed to Steady Source Photons)
θ_0	Initial Phase
$\theta(t)$	Accumulated Phase since the Start of the Observation Interval
$\theta_d(t)$	Doppler Phase
R_s	Flux of the Source Photons (photons/second)
R_b	Flux of the Background Photons (photons/second)
$h(\phi)$	Normalized Pulse Profile Function
f_s	Source Frequency
f	Observed Signal Frequency
f_d	Doppler Frequency Shift
t_0	Time at the Start of the Observation Interval
T_{obs}	Length of the Observation Interval
$\hat{\mathbf{n}}$	Unit Normal Vector Pointing from the SSB to the Pulsar
\mathbf{r}	Position Vector of the Spacecraft with Respect to the SSB
t_{SSB}	Time at the SSB
t_{sc}	Time at the Spacecraft
c	Speed of Light
a	Constant Acceleration Used in the Time-Varying Signal Frequency Scenarios
B_L	Loop Bandwidth of the DPLL
ζ	Damping Ratio of the DPLL
K_1, K_2	Gain Coefficients for the second-order DPLL

List of Figures

1	Image of the Crab Nebula in the Optical and X-ray Spectrums	7
2	Diagram of the Pulse Phase Tracking Concept	12
3	MLE-DPLL Cascade Block Diagram	13
4	Diagram of Spacecraft Orientation and Position with respect to Pulse Wave Fronts Arriving from a Distant Pulsar	13
5	Block Diagram of the Experimental X-ray Photon Generation Process	14
6	Picture of the GXLT Setup	15
7	Sample Oscilloscope Image of XDPG Driving Signal and Photon Arrival Events	15
8	Crab Pulse Profile Template	16
9	B1821-24 Pulse Profile Template	16
10	Example MLE Plot for the Crab Pulsar with Constant Velocity	18
11	Simulation Results Using the Crab Pulsar with a Constant Acceleration Detector Trajectory	19
12	Simulation Results Using B1821-24 with a Constant Acceleration Detector Trajectory	20
13	Experimental Results using the Crab Pulsar with a Constant Detector Acceleration of 0.1 km/s^2	21
14	Experimental Results using B1821-24 with a Constant Detector Acceleration of 0.1 km/s^2	21
15	Experimental Results using the Crab Pulsar with a Constant Detector Acceleration of 5 km/s^2	22

List of Tables

1	Pulsar Parameters for Simulation Runs	16
2	Descriptions of the Performed Simulation Runs	17
3	MLE Results from Simulations	17
4	Pulsar Parameters for Experimental Runs	18
5	Descriptions of the Performed Experimental Runs	19
6	MLE Results from Experiments	20

1 Introduction

Throughout human history, celestial sources have been used as aids for navigation. Most of these sources are constant in emissions, and serve as optical point source references, whose use dates back to ancient sailors navigating by the stars. A small portion of celestial sources emit radiation at varying intensity. This variation allows for new possibilities for use in navigation algorithms that were not achievable with steady point sources. There are many causes of these varying emissions including object pulsations, eruptions, rotation, eclipses by companion stars, and cataclysmic effects [1] [2]. A subset of these varying celestial sources are spinning neutron stars or pulsars. They were first discovered in the radio band in 1967 [3]. Subsequently, pulsars have been discovered that emit radiation throughout the electromagnetic spectrum [4][5]. When it comes to navigation, those that emit in the X-ray band (0.1 - 100 keV) are the most attractive because smaller detectors can be utilized than for optical or radio sources. Figure 1 is an image of the Crab Pulsar in the optical and X-ray bands.

Neutron stars are formed as the result of a supernova explosion of a massive star that has run out of fuel [6] [7]. Conservation of angular momentum spins these stars up to high rates during their collapse. Neutron stars also have very strong magnetic fields, which accelerates charged particles along their field lines [8]. This results in powerful beams of electromagnetic waves, across the entire spectrum, being radiated from the pulsar's magnetic poles. Misalignment between the spin axis and magnetic field axis causes an observer to be able to sense a pulse of magnetic radiation due to the magnetic pole sweeping across the line of sight [8].

Pulsars have very regular, stable and periodic signals [4][5]. In fact they are so stable that some have been shown to match the stabilities of today's atomic clocks [9][10]. Pulsars have unique periodic pulse profiles, which along with their relatively uniform distribution throughout the sky, suggests they might be able to be used as a natural celestial lighthouse system for navigation. The baseline X-ray pulsar-based navigation (XNAV) method uses observations of millisecond period pulsars (MSPs).

Due to their great distance and dispersion, pulsars and XNAV specifically are a method for autonomous navigation in deep space. Some current methods of spacecraft navigation throughout the solar system include: vehicle tracking using the Deep Space Network (DSN) [11], occultation of celestial objects [12], and orbit-determination using Earth-based observations. The primary method is DSN radiometric tracking. This provides a range and range-rate measurement along the line-of-sight from the Earth to the spacecraft. Differential one-way ranging (Delta-DOR) using very long baseline interferometry (VLBI) with the DSN can achieve angular measurements with accuracies on the order of 1 nrad [13]. XNAV measurements have the same accuracy throughout the solar system, whereas measurements from the DSN decrease in accuracy with increasing distance from Earth. Thus, for distant missions, XNAV measurements can either be added to DSN measurements to increase accuracy, or be used alone in order to eliminate the reliance on an uplink from Earth.

Most of the astronomical observation of pulsar sources have been done in the radio band because these emissions can be received on the Earth's surface. This has resulted in suggested methods to use pulsar radio signals for navigation [14], but significant improvement would need to be made in detector technology in order to make this feasible for space missions. Consequently, there is greater focus on methods to observe pulsars in the X-ray band to test a possible XNAV system and provide updated timing models. The All-Sky Monitor (ASM) instrument aboard the Rossi Timing Explorer (RXTE) has served the role of monitoring the X-ray sky in the past [15]. In the future the Neutron-star Interior Composition Explorer (NICER) and Station Explorer for X-ray Timing and Navigation Technology (SEXTANT), in development at the Goddard Space Flight Center (GSFC), will serve these purposes attached to the International Space Station (ISS) [16] [17]. These combined missions will perform phase-resolved spectroscopy of rapidly spinning neutron stars and demonstrate real-time X-ray pulsar navigation using MSPs, respectively.

1.1 Background

A pulsar's timing model can be accurately measured over long observations. These models can be represented as the total accumulated phase of a pulsar's signal over time. An initial signal number Φ_0 is chosen at a fiducial time, t_0 at the Solar System Barycenter (SSB), which is used as an inertial reference location. The total phase can be modeled as a function of time and broken down into fractional and whole integer components [8],

$$\Phi(t) = \phi(t) + N(t), \quad (1)$$

where ϕ is the fractional portion of the pulse period and N is the number of integer cycles since t_0 . This can also be expressed in terms of the pulse signal frequency and its derivatives. This is known as the pulsar spin equation [8],

$$\Phi(t) = \Phi(t_0) + f[t - t_0] + \frac{\dot{f}}{2}[t - t_0]^2 + \frac{\ddot{f}}{6}[t - t_0]^3. \quad (2)$$



Figure 1: On the Left is an image of the Crab Nebula and Pulsar, in the optical (red) and X-ray (blue) portions of the spectrum superimposed. The right image is the Crab Pulsar in only the X-ray portion of the spectrum (NASA/CXC/ASU/J. Hester et al.) [18].

In order to be used in navigation, pulsars need to be accurately modeled and identified. Previous methods of determining a pulsar source's characteristics have relied on creating binned pulse profiles over long observations of a source and then folding back over the expected pulse period [1]. Observed pulse time of arrivals (TOAs) are then computed through comparison with a high signal-to-noise ratio (SNR) template. The pulse signal needs to be accurately timed over each observation with respect to an inertial system. This time transformation must be done carefully to avoid a smearing effect that would be present if removal of the motion and higher order Doppler effects is done incorrectly, causing increased navigation errors [1]. Various methods for position determination have been studied in the literature [19], [20], [21], [22] [23], and [24]. These approaches fall in two general categories: absolute 3-dimensional position and velocity determination in an inertial frame, and delta-correction where estimates of range and range-rate values are updated. Both methods provide the means to maintain a continuous navigation solution [8].

1.2 Suggested Approach

The approach used in this paper is modeled after the pulse phase tracking algorithm that was developed in [1]. This method attempts to exploit the periodic nature of pulsars by measuring the pulse TOAs onboard a moving spacecraft. The pulse phase measured on the spacecraft depends on the radial distance between the spacecraft and the pulsar. Thus, information about the spacecraft's position can be extracted from these measurements. The practicality of using this for navigation purposes was looked at in the radio band in [19] [25] [26] and in the X-ray band in [24] [25] [27].

The method of phase tracking relies on the use of a maximum-likelihood phase estimator (MLE), which can estimate the initial phase at the beginning of an observation of a pulsar given a set of TOAs over that interval. When the signal frequency is constant at the spacecraft this measurement of the initial phase is enough to know the phase evolution over the entire observation time interval since it changes linearly with known slope. In the case of changing signal frequency, due to the dynamical motion of the spacecraft, the observation window can be broken up into smaller blocks over which the frequency can be assumed constant. Then the phase of the observed pulse can be tracked over the observation as the spacecraft travels along its trajectory, which gives a measure of distance and range rate [1]. The output of the MLE in this case is sent through a digital phase-locked loop filter (DPLL) at each iteration in order to reduce the errors. An advantage of this method is that, if it is used as a delta-correction technique, it can possibly provide continuously updating position information as opposed to the infrequent TOA-difference technique [8].

The proposed method tracks the expected parameters of the source signal in order to estimate the spacecraft trajectory. This allows continuous updates of the vehicle motion over short time frames. An added advantage of phase tracking is that it eliminates the requirement of time transferring all of the photons arriving at the spacecraft to an inertial reference at the SSB before measurements can take place. This eliminates the risk of smearing the phase profile over the time transfer. This phase tracking algorithm was demonstrated through simulation in [1] by

looking at an RXTE observation of the Crab pulsar. The algorithm was shown to have good phase and frequency tracking capabilities. The goal of this paper is to experimentally validate this phase tracking algorithm using a lab setup that includes a modulated X-ray source to emit photons that model those arriving from a pulsar and a detector to read and time-tag the collection of the emitted X-ray photons. This setup was then used to perform phase tracking on the received TOAs at the detector in the lab. This adds the complexity of dealing with actual photons and detector physics outside of the simulation environment. This method was tested over various scenarios over a range of constant and changing signal frequency cases. Both the Crab pulsar (B0531+21) and B1821-24 were used as source models and the results were compared to simulations.

2 X-Ray Pulsar Signal Model

2.1 Non-Homogeneous Poisson Process

Due to the periodic nature of pulsar signals, the time of arrivals of X-ray photons at a spacecraft detector can be modeled as a non-homogeneous Poisson process (NHPP)[1]. With this assumption, the number of photons arriving from a pulsar in a given interval is a Poisson random variable with a periodic or possibly quasi-periodic rate function $\lambda(t) \geq 0$. Given this model, the probability that k photons arrive from a source in an interval (a, b) is given by the following [1][28],

$$\Pr[k; (a, b)] = \frac{1}{k!} \{ \exp[-\int_a^b \lambda(t) dt] \} [\int_a^b \lambda(t) dt]^k. \quad (3)$$

The rate function $\lambda(t)$ is a cumulation of all photons that hit the detector. This includes both the source photons, which arrive at an average rate of R_s photons per second (ph/s) and the background photons arriving at the constant rate R_b ph/s [1]. The source photons include both pulsed and steady emissions from the pulsar, and the pulse fraction ρ gives their ratio. The non-pulsed source photons behave like background photons, which makes it difficult to tell them apart at the spacecraft detector. The following consequences stem from the use of the NHPP model [1]:

1. Setting $k = 0$ in Equation (3) gives the probability that zero photons will arrive in (a, b)

$$\Pr[0; (a, b)] = \exp[-\int_a^b \lambda(t) dt] \quad (4)$$

2. The Probability that exactly one photon arrives in an infinitesimal interval of length Δt centered at time t is given by evaluating Equation (3) with $k = 1$

$$\Pr[1; (-\Delta t/2, +\Delta t/2)] = \lambda(t; \theta_0, f) \Delta t \quad \text{as } \Delta t \rightarrow 0, \quad (5)$$

where $\lambda(t; \theta_0, f)$ is the rate function given in terms of the initial phase and frequency parameters, which will be discussed later.

3. The Probability of more than one photon arriving in an infinitesimal interval of length Δt is zero when $\Delta t \rightarrow 0$.
4. The number of photons arriving in a given interval is independent from those of all other disjoint intervals.

2.2 Pulsar Rate Function

The time-varying rate of arrival of the pulsed source photons can be modeled as the composition of the normalized pulse profile function, $h(\phi)$, and observed phase at the spacecraft detector, $\phi_{det}(t)$ [1]. This, along with the notion of constant rate background and non-pulsed source photons, allows us to write the overall rate function for a given pulsar as [1]

$$\lambda(t) = R_b + (1 - \rho)R_s + \rho R_s h(\phi_{det}(t)) \quad (ph/s). \quad (6)$$

We can define parameters α and β , called the effective source and background photon arrival rates, as follows

$$\alpha = \rho R_s \quad (ph/s) \quad (7)$$

$$\beta = R_b + (1 - \rho)R_s \quad (ph/s). \quad (8)$$

These parameters capture the flux of the periodic source photons and the constant flux of the cumulation of the background and non-pulsed source photons, respectively. They are important for considering performance, and their ratio corresponds to the signal-to-noise ratio (SNR) of the pulsar with a particular detector setup.

The pulse profile function $h(\phi)$ is normalized to satisfy the conditions:

1. $\min_{\phi \in (0,1)} h(\phi) = 0$
2. $\int_0^1 h(\phi) d\phi = 1$.

Usually, h is defined for $\phi \in (0,1)$, but in order to be used in Equation (6) it needs to be extended as a periodic function with a period of one cycle. This can be done by letting $h(m + \phi) = h(\phi) \forall m \in \mathbb{Z}$ [1]. Then h is defined for $\phi \in (-\infty, +\infty)$, which allows $h(\phi_{det}(t))$ to continue to be computed in Equation (6) even as the phase accumulated at the detector grows over the observation interval.

Now, define the phase observed at the detector as the sum of the initial phase, θ_0 , and the accumulation of phase since the start of the observation period, $\theta(t)$. Then in terms of the observed signal frequency, $f(t)$, the accumulated phase at the detector over an observation interval (t_0, t) is given as

$$\phi_{det}(t) \equiv \theta_0 + \theta(t) = \theta_0 + \int_{t_0}^t f(t') dt'. \quad (9)$$

The observed signal frequency can be broken up into source frequency and doppler frequency componenets [1]:

$$f(t) = f_s + f_d(t) = f_s(1 + v(t)/c), \quad (10)$$

where the doppler frequency shift is $f_d = f_s v(t)/c$, $v(t)$ is the range rate of the spacecraft in the line-of-sight direction to the pulsar, and c is the speed of light.

For the sake of this paper, the source frequency, f_s , is taken as constant on the observation interval, and the second and higher-order relativistic doppler effects are ignored. Under these assumptions, the pulsar spin equation, Equation (2), simplies to Equation (9). This will allow for the development of a Maximum-Likelihood Estimator and Phase-Tracking Algorithm as in [1]. As explained in [1], the scope of analysis is not limited by these assumptions since source frequency variations are often forecasted, which allows for pre-processing of the photon TOA measurements to remove the effects due to these changes.

Under these assumptions, the phase accumulated since the beginning of the observation has two terms [1],

$$\theta(t) = f_s(t - t_0) + \int_{t_0}^t f_d(t') dt', \quad (11)$$

where $\theta_d(t) = \int_{t_0}^t f_d(t') dt'$ is the doppler phase. If range-rate $v(t)$ is a constant v , $\theta(t) = f_s(1 + v/c)(t - t_0)$ is linear and thus the Poisson rate function $\lambda(t)$ is periodic. For non-constant range-rate, the Poisson rate function is only quasi-periodic due to the nonlinear dependence of $\theta_d(t)$ on time. The cases of constant and time-varying observed signal frequency can be considered and dealt with separately. Now look at the rate function under each scenario.

2.2.1 Constant Observed Signal Frequency

First, notice that with constant observed signal frequency, $f = f_s(1 + v/c)$, the phase at the detector is given linearly as follows [1],

$$\phi_{det} = \theta_0 + f(t - t_0). \quad (12)$$

Solve for the Poisson rate function by substituting Equation (12) into Equation (6), which gives

$$\lambda(t; \theta_0, f) = \beta + \alpha h(\theta_0 + f(t - t_0)). \quad (13)$$

This shows the functional dependence of the rate function on θ_0 and f and that λ is strictly-periodic due to the periodicity of h . When the detector is stationary or is moving at a constant range-rate with respect to the pulsar, the constant signal frequency model can be used. Also, the period change of the pulsar over the observation time interval should be negligible[1].

2.2.2 Time-Varying Observed Signal Frequency

The observed phase at the detector has a term contributed by the doppler effects when the frequency is varying [1]. In this case,

$$\phi_{det} = \theta_0 + \int_{t_0}^t f(t')dt' = \theta_0 + \int_{t_0}^t [f_s + f_d(t')]dt' = \theta_0 + f_s(t - t_0) + \theta_d(t). \quad (14)$$

Now plug this into Equation (6) to get the quasi-periodic Poisson rate function for the time-varying frequency case

$$\lambda(t) = \beta + \alpha h(\theta_0 + f_s(t - t_0) + \theta_d(t)). \quad (15)$$

This model must be used if the radial speed with respect to the pulsar is varying considerably over the observation interval.

3 Maximum-Likelihood Initial Phase and Frequency Estimation

Now the Maximum-Likelihood Estimator (MLE) for θ_0 and f can be derived following the approach of [29] and [1] for the constant frequency model. The goal is to estimate these parameters based on a set of TOAs, which are either a computer simulated realization of the NHPP or an experimentally detected realization of the NHPP. For background on MLEs [29], [30], and [31] were consulted.

Assume that the pulse profile function $h(\phi)$, effective source arrival rate α , and effective background arrival rate β are all known. Consider an observation interval $(t_0, t_0 + T_{obs})$ and a set of photon TOAs $\{t_k\}_{k=0}^K$ with $t_0 < t_k < t_0 + T_{obs} \forall k$. These TOAs are a realization of the NHPP for the pulsar with rate function $\lambda(t; \theta_0, f)$ given by Equation (13). The aim is to estimate the model parameters θ_0 and f .

The first step is to compute the K-dimensional joint probability density function (pdf) of the NHPP realization, $f(\{t_k\})$. This is achieved by considering infinitesimal intervals of length Δt_k centered around each $t_k, k = 1, 2, \dots, K$. The joint pdf can be computed by first looking at the probability that one and only one photon arrives within each interval and none outside of them [1]

$$\begin{aligned} f(\{t_k\})\Delta t_1\Delta t_2\cdots\Delta t_K &= \Pr[0; (t_0, t_1 - \Delta t_1/2)] \times \Pr[1; (t_1 - \Delta t_1/2, t_1 + \Delta t_1/2)] \\ &\times \Pr[0; (t_1 + \Delta t_1/2, t_1 - \Delta t_1/2)] \times \cdots \times \Pr[1; (t_K - \Delta t_K/2, t_K + \Delta t_K/2)] \\ &\times \Pr[0; (t_K + \Delta t_K/2, t_0 + T_{obs})]. \end{aligned} \quad (16)$$

From the consequences of the NHPP model plug in Equations (4) and (5). Now take $\Delta t_k \rightarrow 0$ for all $1 \leq k \leq K$. This yields,

$$f(\{t_k\}) = \exp \left[- \int_{t_0}^{t_0 + T_{obs}} \lambda(t; \theta_0, f) dt \right] \prod_{k=1}^K \lambda(t_k; \theta_0, f), \quad (17)$$

which is the likelihood function [1]. The desired MLE solves for the values of θ_0 and f at which the likelihood function is maximized. It is equivalent to consider the logarithm of the likelihood function (LLF), which is easier to minimize,

$$LLF(\tilde{\theta}_0, \tilde{f}) \equiv \sum_{k=1}^K \log[\lambda(t_k; \tilde{\theta}_0, \tilde{f})] - \int_{t_0}^{t_0 + T_{obs}} \lambda(t; \tilde{\theta}_0, \tilde{f}) dt. \quad (18)$$

Here log is the natural logarithm, and $\tilde{\theta}_0$ and \tilde{f} are the values at which the LLF is computed. In most cases, the integral in Equation (18) can be dropped since it displays a minimal dependence on the search model parameters. This minimal dependence holds when the observation interval lasts many cycles of the signal at the expected frequency ($\tilde{f}T_{obs} \gg 1$) [1]. The optimization problem that needs to be solved by the MLE is:

$$(\hat{\theta}_0, \hat{f}) = \underset{\tilde{\theta}_0 \in \Theta, \tilde{f} \in \Omega}{\operatorname{argmax}} \sum_{k=1}^K \log[\beta + \alpha h(\tilde{\theta}_0 + \tilde{f}(t_k - t_0))], \quad (19)$$

where Θ and Ω are the search spaces for phase and frequency, respectively. Solving this maximization by brute-force involves nested, iterative grid-searches. Each iteration searches a smaller region, but with greater precision around the output of the previous iteration. The simulation methods used specifically for this paper will be discussed in a

later section. There are also more sophisticated methods that attempt to decrease the MLE run time. For example [32] uses a Discrete Fourier Transform procedure to increase speed, but it sacrifices the guarantee that the output is a maximum.

If it is assumed that the signal frequency and doppler shift are known, then Equation (19) reduces to a phase-only optimization,

$$\hat{\theta}_0 = \underset{\tilde{\theta}_0 \in \Theta}{\operatorname{argmax}} LLF(\tilde{\theta}_0, f_{ref}), \quad (20)$$

where f_{ref} is the a-priori known signal frequency. It was shown in [1] that the performance of this MLE is optimal since it achieves the Cramer-Rao performance bound after a certain threshold. If the observed signal frequency is constant, the measurement of the initial phase θ_0 by the MLE and knowledge of the frequency f , either a-priori or from the MLE, is sufficient to determine the phase over the entire observation interval. This is because the phase at the detector has a linear dependence on θ_0 and f if the signal frequency is constant, as seen in Equation (12).

4 Pulse Phase Tracking

When observations are made onboard a spacecraft whose trajectory curves with respect to the pulsar, or the radial speed in the direction of the source varies by a noticeable amount, then the observed frequency can no longer be considered constant without accruing errors that will overwhelm the navigation scheme. The procedure of pulse phase tracking of [1] will be adopted to deal with this. This is based on the time-varying signal frequency model introduced in Section 1.2.2. The first step is to partition the observation interval into N blocks of size T , which is set small enough so that the observed signal frequency is approximately constant over each block. This is illustrated in Figure 2. Photons arriving in the n -th block are processed in a batch using the MLE of Equation (20) to solve for the y-intercept $\hat{\theta}_0(n)$ as seen in Figure 2. When the reference frequency is equal to the source frequency, $\hat{\theta}_0(n)$ is an estimate of $\theta_0 + \theta_d(t)$ for $t = nT$. Thus, by using MLEs over one block of photon TOAs at a time, this algorithm tracks the phase quantity $\theta_0 + \theta_d(t)$ over the entire observation interval [1].

There are a few issues that need to be addressed with regards to implementing this phase tracking algorithm. First, the sequence of estimates $\hat{\theta}_0(n)$ may contain jumps due to phase wraparounds. In order to deal with this, the search space for the first block will be the entire phase space $\Theta = (0, 1)$, but subsequent blocks will take the previous block's phase estimate $\hat{\theta}_0(n-1)$ as the center of the search window. This allows the sequence $\hat{\theta}_0(n)$ to wander outside of $(0, 1)$, if necessary, to avoid jumps. The other main issue is the presence of noise due to unmodeled vehicle dynamics and estimation errors. To reduce these effects, the sequence of outputs $\hat{\theta}_0(n)$ from the MLE can be post-processed through a digital phase-locked loop (DPLL). This allows for a sequence of estimates $\hat{\theta}_0^{DPLL}(n)$ and $\hat{f}_d^{DPLL}(n)$ to track the phase and doppler frequency with smaller errors than using the MLE alone.

4.1 Digital Phase-Locked Loops

A digital phase-locked loop (DPLL) filter can be used to reduce the effects of the inherent estimation errors and noise in the MLE phase outputs $\hat{\theta}_0(n)$ [1]. Phase-Locked Loops are abundant in modern signal processing and communication systems [33]. The idea is to be able to form a local representation that is synchronized with an incoming signal's frequency and phase. An overview of phase-locked loop techniques is included in [34]. Originally, all phase-locked loops were analog, and their implementation and design relied extensively on knowledge of analog systems [35]. Techniques for designing and implementing analog phase-locked loops are discussed in [36] and [37]. In order to take advantage of advances in digital computing, fully digital loops have been developed. DPLLs have increased in popularity due to advantages with respect to performance, speed, reliability, size, and cost [33]. Also, DPLLs allow for their parameters to be defined such that each has a direct physical meaning with respect to loop noise bandwidth B_L , root-specific decay rate, or root-specific damping [38]. Digital Phase-Locked loop design and implementation are discussed at length in [33].

The second-order DPLL used in [1] and developed in [38] will be presented and used in the pulse phase tracking algorithm. This formulation allows the loop-filter constants to be determined from loop roots that can be placed anywhere in the complex plane [38]. The DPLL will be implemented in a cascade with an MLE as seen in Figure 3. Thus, it is assumed that the photon TOAs arriving at the detector are first processed through the MLE, which gives an estimate $\hat{\theta}_0^{MLE}(n)$ at each block. The reference frequency used in the MLE is set equal to the source frequency, which is assumed constant, $f_{ref} = f_s$. Now the algorithm for the second-order DPLL will be presented. The first step is to compute the difference between the input phase from the MLE and the DPLL's phase estimate. This is done through the following ideal phase detector,

$$\tilde{\phi}(n) = \hat{\theta}_0^{MLE}(n) - \hat{\theta}_0^{DPLL}(n). \quad (21)$$

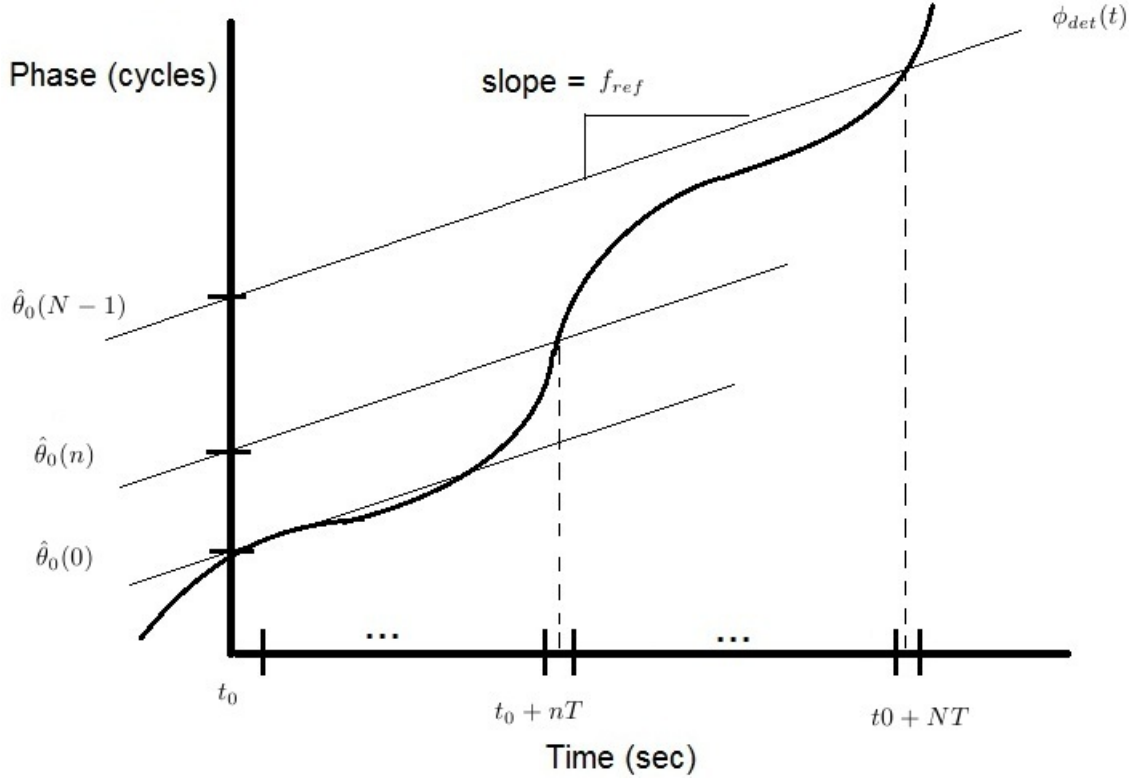


Figure 2: This diagram demonstrates the pulse phase tracking concept presented in [1]. The observation interval is broken up into N blocks of size T seconds over which the signal frequency is approximately constant.

This is carried out without wrapping around the phase. Next, the state of the loop filter can be updated using the error feedback $\tilde{\phi}(n)$ [38]

$$\hat{f}_d^{DPLL}(n+1)T = K_1 \tilde{\phi}(n) + K_2 \sum_{m=1}^n \tilde{\phi}(m), \quad (22)$$

where \hat{f}_d^{DPLL} is the measurement of the doppler phase by the DPLL and T is the loop update interval, which is set equal to the block duration of the phase tracking algorithm. This sequence, $\hat{f}_d^{DPLL}(n+1)T$, drives a numerically controlled oscillator (NCO), which sets the amount the current NCO phase must be changed in order to achieve the phase estimate of the next block. The NCO corresponds to the following phase accumulation at baseband,

$$\hat{\theta}_0^{DPLL}(n+1) = \hat{\theta}_0^{DPLL}(n) + \hat{f}_d^{DPLL}(n+1)T. \quad (23)$$

In order to initialize the phase and frequency states of the DPLL before the start of the loop take $\hat{\theta}_0^{DPLL}(0) = \hat{\theta}_0^{MLE}(0)$ and $\hat{f}_d^{DPLL}(0) = f_s \hat{v}(t_0)/c$. If there is not an available estimate of the initial range rate $\hat{v}(t_0)$ set $\hat{f}_d^{DPLL}(0) = 0$.

5 Simulation Structure

First, the MLE and pulse phase tracking MLE-DPLL cascade were tested in a computer simulation environment using MATLAB. In this case the photon TOAs received by a detector are generated by a realization of the NHPP with rate function given by Equation (6). This set of TOAs is first generated as if they are located at the solar system barycenter (SSB) and then delay is added in order to account for the offset between the detector and the SSB. The NHPP photon generation is completed using the inversion method of non-uniform random variate generation presented in [39] and implemented for the specific example of X-ray pulsar photon generation in [40]. The general relativistic delay and doppler effects must be taken into account to transfer the barycentric set of time of arrivals to

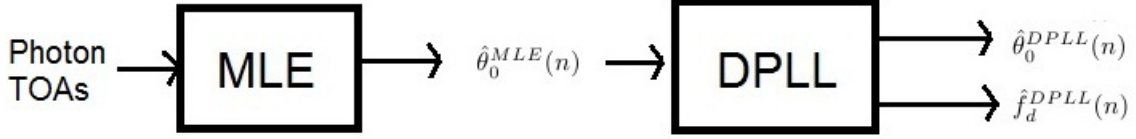


Figure 3: This figure shows the MLE-DPLL cascade used to reduce errors in the pulse phase tracking algorithm when the observed signal frequency is time-varying [1].

a set arriving at the spacecraft detector, which is desired to test the algorithms. To first order, this time transfer is given by

$$t_{SSB} - t_{sc} = \frac{\hat{\mathbf{n}} \cdot \mathbf{r}}{c}, \quad (24)$$

where t_{SSB} is the time at the SSB, t_{sc} is the time at the spacecraft, $\hat{\mathbf{n}}$ is the unit normal vector pointing from the SSB to the pulsar, and \mathbf{r} is the position vector of the spacecraft with respect to the SSB, as seen in Figure 4 [41]. This set of TOAs at the spacecraft detector is what is sent to the MLE or MLE-DPLL cascade algorithms.

In the constant signal frequency case the MLE algorithm is run one time using all of the TOAs in the entire observation interval. This results in estimates for the phase at the detector at all times in the observation, because it is given linearly by Equation(12) and the MLE gives estimates of the unknown model parameters. This method is used to test both cases where the detector is stationary and where the detector is moving with a constant range rate with respect to the pulsar. When the signal frequency is time-varying the observation interval is broken up into blocks and the pulse phase tracking algorithm is used along with the MLE-DPLL cascade structure.

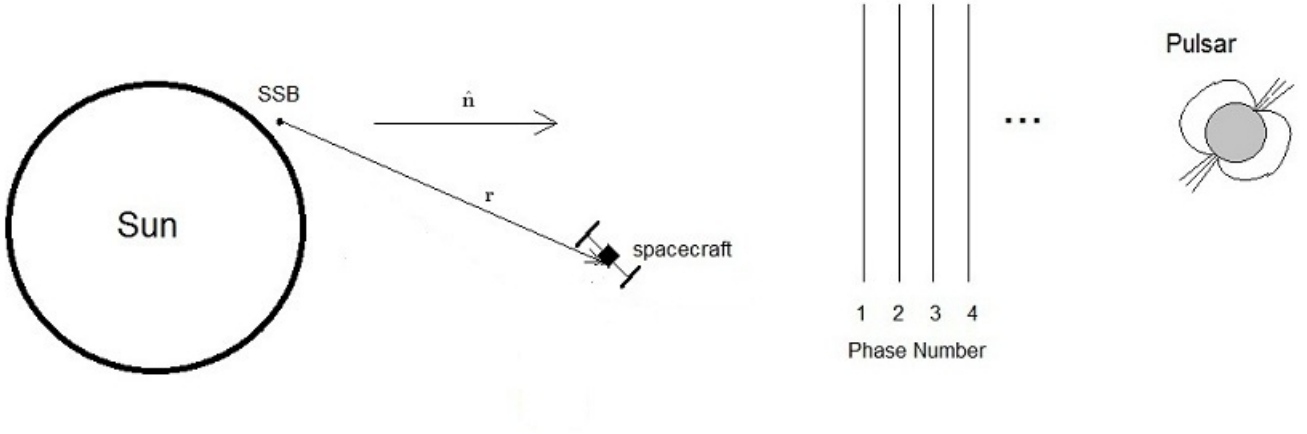


Figure 4: This figure shows the relationship between the spacecraft position, the SSB, and the pulses arriving from the distant pulsar, which can be assumed to be arriving as uniform wave fronts throughout the solar system [41].

6 Experimental Procedure

The main goal of this paper is to experimentally validate the phase-tracking algorithm. The lab equipment of the NICER and SEXTANT teams at the NASA Goddard Space Flight Center (GSFC) was used for this purpose.

The GSFC X-ray Navigation Laboratory Testbed (GXLT), that the SEXTANT mission team used for their own development, was ideal for testing the algorithms discussed in this paper. The GXLT is made up of four major components: the X-Ray Digital Pulse Generator (XDPG), which creates a real-time implementation of the pulsar rate signal given in Equation (6), the Modulated X-Ray Source (MXS), which emits the X-ray photons, the Silicon Drift Detector (SDD), which receives the photons and produces a single short pulse using a pulse shaping filter, and the Time-Tagging X-Ray Detector (XDET), which puts a time stamp on the photon pulses from the SDD [17]. The XDPG takes the pulsar definition and the desired phase dynamics and creates a real-time implementation of the rate-function at the spacecraft and then drives the input of the MXS as an NHPP [17]. Figure 5 illustrates the interconnections of the lab equipment and their use in generating the desired X-ray photons.

The MXS is discussed in [42], and it uses an Ultraviolet (UV) Light Emitting Diode (LED) to modulate, through photoelectron flux, the X-ray photon emissions [17]. This choice of source allows for better modeling of MSP X-ray photons because it allows for fast switching response, intensity control, and is completely off when switched off [42]. Other common X-ray sources lack some of these requirements. Analysis of the SDD is included in [43]. The choice to use an SDD by the NICER team was due to its processing excellent energy resolution, operational simplicity, and fairly good time resolution [43]. Figure 6 contains a picture of the lab setup during a run. The oscilloscope shows the shape of the desired pulse profile as well as an output of the photons as they arrive at the detector. The MXS is commanded to emit photons that model TOAs received at the desired spacecraft location. This produces a set of TOAs received by the SDD that corresponds to photons the detector would see if it was traveling on the desired trajectory. The output of the SDD is sent through a pulse shaping filter, which produces a Gaussian pulse-like voltage signal [17]. This signal can be observed on an oscilloscope, as in Figure 7, in order to see the arrival rate matches the XDPG driving signal.

Although this procedure uses artificially generated photons from an MXS instead of actual detection of a pulsar signal in the X-ray band, it still provides the added complexity and noise related to generating actual X-rays and detecting them with an SDD. This is a step above the purely computer simulated results because it includes the processing of X-ray TOAs at a detector, which was unaccounted for in the simulation. The output no longer automatically matches the realization of the NHPP. The same test situations for the computer simulations were used with the experimental equipment, and the results were compared.

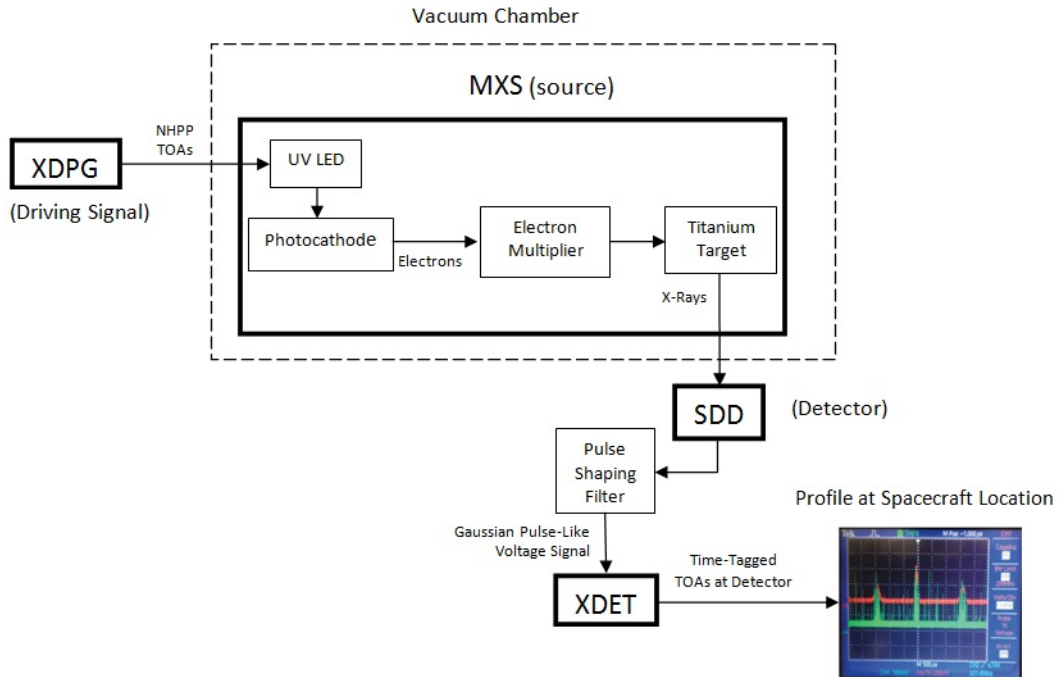


Figure 5: This is a diagram demonstrating how the XDPG, MXS, SDD, and XDET work together to generate and detect the desired X-ray photons. The internal workings of the X-ray generation process performed by the MXS is included. The oscilloscope output image is taken from [17].

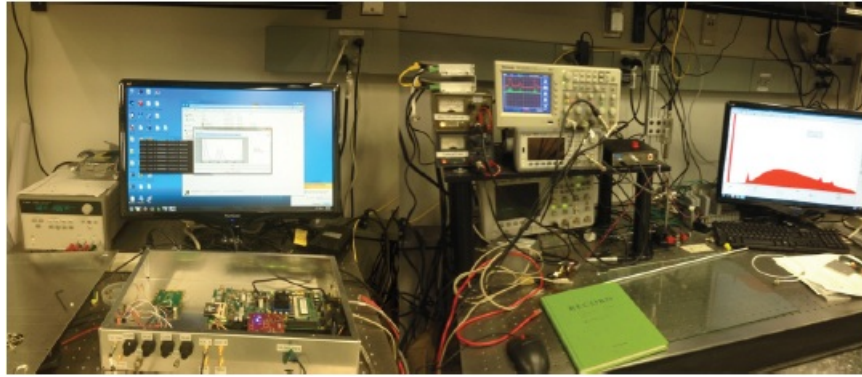


Figure 6: This is a picture of the lab setup for the X-ray navigation ground testbed in use by the NICER team at GSFC. Image taken from [17].

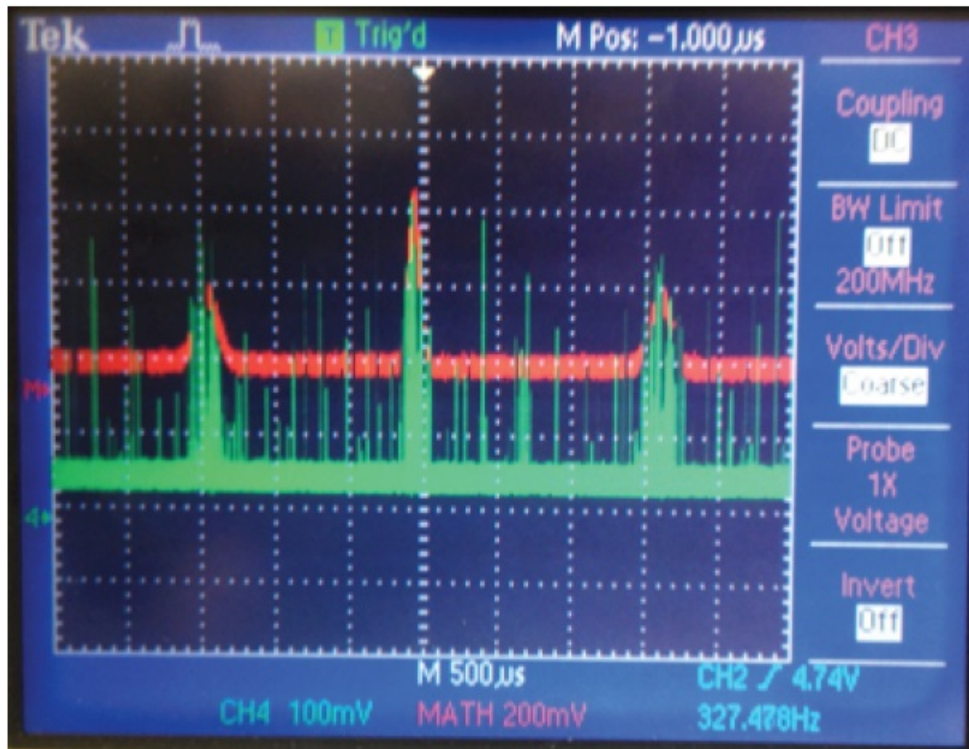


Figure 7: This image shows the XDPG driving signal in red and the corresponding photon arrival events at the SDD for a low SNR. Image taken from [17].

7 Results and Discussion

7.1 Simulation Results

The pulsars that were used to test the phase tracking algorithms with simulations were B0531+21, the Crab pulsar, and B1821-24. The parameters for each of these pulsars that were used for the simulations are given in Table 1. An amplified version of B1821-24 needed to be used to implement the phase tracking by blocks algorithm, since otherwise the flux was too low for a sufficient number of photons to arrive in each block. This artificial amplification is for the purpose of demonstrating the validity of the algorithm and attempts at a more realistic implementation, over a wider range of pulsars, will be investigated in future work. The amplified version of B1821-24 was also used for the constant frequency MLE cases. This was in order to make the observation times be equal to those used for the Crab pulsar. Figures 8 and 9 contain the pulsar pulse profile templates that were used to model the Crab pulsar and B1821-24, respectively.

Table 1: Pulsar Parameters for Simulation Runs

Pulsar	fs (Hz)	α (ph/s)	β (ph/s)
B0531+21 (Crab)	29.9401	1078	462
B1821-24	327.86885	0.18914	0.00386
B1821-24 amplified	327.86885	1470	30

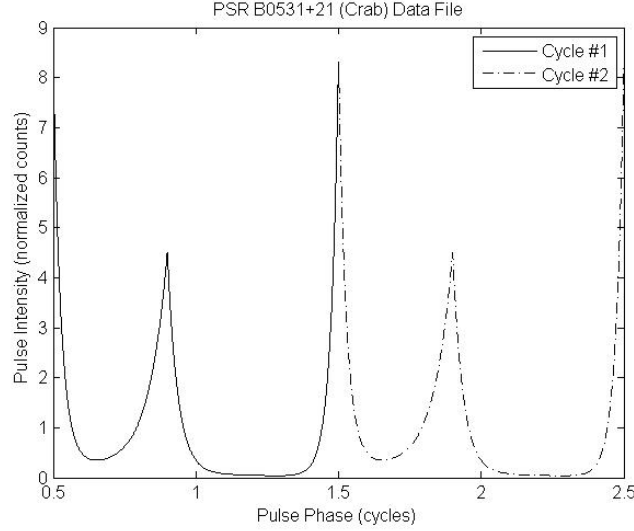


Figure 8: This is the template for the Crab pulsar profile used in the simulations, shown over two periods.

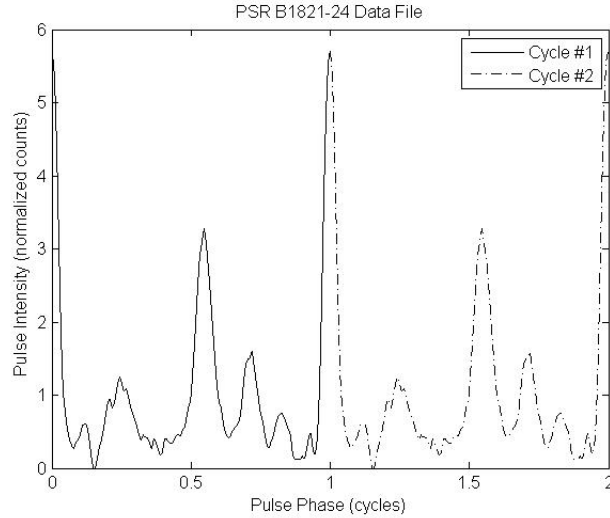


Figure 9: This is the template for the pulse profile of B1821-24 used in the simulations, shown over two periods.

Simulations were developed around three basic scenarios in order to test the phase tracking algorithms. Two fall under the constant signal frequency model and the third requires the signal frequency to be considered time-varying. All three assume a one-dimensional orbit determination problem, the spacecraft is moving along the line-of-sight direction to the pulsar. This simplification allows the orbit information for the spacecraft to be easily determined and reduces the complexity of the problem, so it is easier to focus on the performance of the phase tracking algorithms. Future work will expand this to three-dimensional orbits. The two constant signal frequency scenarios considered were a stationary detector and a detector moving at a constant velocity. For the time-varying frequency scenario, the spacecraft is taken to be moving with a constant acceleration. These cases all allow for easy analytical determination of the truth trajectories for the phase at the detector. For instance, we know that in the constant signal frequency

case, the phase evolves linearly at the detector and thus the truth trajectory is determined completely by the initial phase θ_0 and the observed signal frequency $f = f_s(1 + v/c)$. For the time-varying signal frequency case with constant acceleration a , the doppler frequency shift is given by

$$f_d(t) = f_s \frac{v_0 + at}{c}. \quad (25)$$

This can then be integrated in Equation (14) to give the phase at the detector

$$\phi_{det}(t) = \theta_0 + f_s(t - t_0) + \frac{f_s}{c}[v_0(t - t_0) + \frac{a}{2}(t - t_0)^2]. \quad (26)$$

The phase tracking algorithm provides estimates of $\phi_{det}(t) - f_s(t - t_0)$, so the truth trajectory for the constant acceleration case is

$$\theta_0(t) = \theta_0 + \frac{f_s}{c}[v_0(t - t_0) + \frac{a}{2}(t - t_0)^2]. \quad (27)$$

Table 2 lists all of the different simulations that were run along with their parameters. For the constant signal frequency cases the TOAs were processed through the MLE of Equation (20) in order to give estimates $\hat{\theta}_0$. For each simulation Monte-Carlo methods were used on ten repeated trials in order to attempt to remove some of the affects due to non-deterministic effects, such as noise, on the accuracy of the MLE algorithm. The results for the stationary and constant velocity cases are presented in Table 3. The simulated results all had less than 0.15 % error from the true initial phase of $\theta_0 = 0.5$. An example of an MLE plot for one of the scenarios is provided in Figure 10.

Table 2: Descriptions of the Performed Simulation Runs

Pulsar	Type of Run	θ_0	v_0 (km/s)	a (km/s ²)	Initial f_d (hz)	Number of Runs	Observation Time (sec)
Crab	Stationary	0.5	0	0	29.9401	10	10
B1821-24	Stationary	0.5	0	0	327.86885	10	10
Crab	Constant v	0.5	0.1	0	29.9402	10	10
B1821-24	Constant v	0.5	0.1	0	327.86995	10	10
Crab	Constant a	0.3	0	0.1	29.9401	1	200
B1821-24	Constant a	0.3	0	0.1	327.86885	1	200

Table 3: MLE Results from Simulations

Pulsar	Type of Run	Average θ_0	Percent Error
Crab	Stationary	0.500145	0.029
B1821-24	Stationary	0.499825	0.035
Crab	Constant V	0.50012	0.024
B1821-24	Constant V	0.500745	0.149

For the time-varying frequency cases, with constant acceleration, the TOAs arriving at the spacecraft detector were broken up into blocks of size $T = 1$ second. The MLE-DPLL cascade was then applied to track the phase. The loop bandwidth was taken to be $B_L = 0.05$ Hz and the damping ratio was set at $\zeta = 0.707$, which is the standard underdamped response. The gain coefficients K_1 and K_2 for the second-order DPLL were chosen from Table VI in [38]. This resulted in $K_1 = 0.1199$ and $K_2 = 0.007658$. The loop phase and frequency states were initiated using $\hat{\theta}_0^{DPLL}(0) = \hat{\theta}_0^{MLE}(0)$ and $\hat{f}_d^{DPLL}(0) = f_s \hat{v}(t_0)/c$.

Figure 11 contains the results for the simulated phase tracking using the Crab pulsar with a constant acceleration as given in Table 2. The top plots show the phase outputs of the MLE algorithm and the MLE-DPLL algorithm along with the truth trajectory. It can be seen that they both track the true phase over the observation window, but the error is smaller for the DPLL phase as expected. The bottom two plots show the DPLL frequency state versus the true frequency evolution and the error. The DPLL frequency is tracking with some fluxuations, but with an error on the order of 10^{-4} . Figure 12 contains the results for the simulated phase tracking using pulsar B1821-24 with a constant acceleration as given in Table 2. The top plots show the phase outputs of the MLE algorithm and the MLE-DPLL algorithm along with the truth trajectory. It can be seen that they both track the true phase over the observation window, but the error grows linearly as the observation time increases. The error is reduced in the DPLL output over the MLE output as expected, but both errors grow without an apparant bound. This might

be due to the non-zero acceleration and a third order DPLL might need to be considered in future research if the phase error is getting out of hand. The bottom two plots show the DPLL frequency state versus the true frequency evolution and the error. The DPLL frequency is tracking with some fluxuations, but with an error on the order of 10^{-3} .

7.2 Experimental Results

The same pulsars were used for the experimental runs, using the GXLT, as were used in the computer simulations. The effective source and background fluxes are different and the frequency for B1821-24 is slightly different in the model used in the GXLT versus the computer simulations. These parameters are all included in Table 4. An amplified version of B1821-24 was again used in order to implement the phase tracking algorithm for time-varying frequency.

Table 4: Pulsar Parameters for Experimental Runs

Pulsar	fs (Hz)	alpha (ph/s)	beta (ph/s)
B0531+31 (Crab)	29.9401	190	1510
B1821-24	327.405595	0.083	0.41
B1821-24 amplified	327.405595	1500	100

Experimental runs were designed around the same basic three scenarios as with the computer simulations. Table 5 contains a list of descriptions of all the experimental runs performed. Once again for each of the constant signal frequency cases, ten seperate runs were completed and their results were combined with Monte-Carlo methods to reduce the chance the performance was an outlier due to non-deterministic noise. The truth trajectories for each constant acceleration case were the same as they were for the computer simulations. One extra experiment was carried out using the Crab pulsar with a detector moving at a constant acceleration of 5 km/s^2 with an initial velocity of 1 km/s and an initial phase of 0.5 . The goal was to determine if the phase-tracking algorithm could still adequately track the trajectory even with a significantly higher acceleration. This was tested using the crab pulsar due to it's higher flux than B1821-24.

The results obtained from using the MLE to estimate the initial phase for the stationary and constant velocity cases are contained in Table 6. The results all had less than 2.5% error from the true initial phase of $\theta_0 = 0.5$. The spacecraft TOAs obtained in the constant acceleration case were processed, as in the computer simulations, by the MLE-DPLL cascade with a block size of $T = 1$ second. The gains and parameters for the DPLL were all taken to be the same as in the simulations. Figure 13 contains the results for the experimental phase tracking using the Crab pulsar with a constant acceleration as given in Table 5. The top plots show the phase outputs of the MLE algorithm

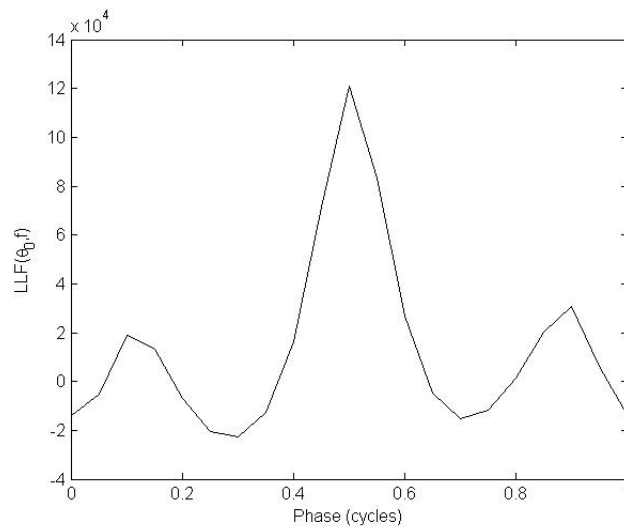


Figure 10: This is an example of an MLE plot for the crab pulsar with constant velocity $v = 1 \text{ km/s}$ and initial phase $\theta_0 = 0.5$. It is seen that the peak is near 0.5 as desired and the MLE gave an output of $\hat{\theta}_0 = 0.50035$ in this case.

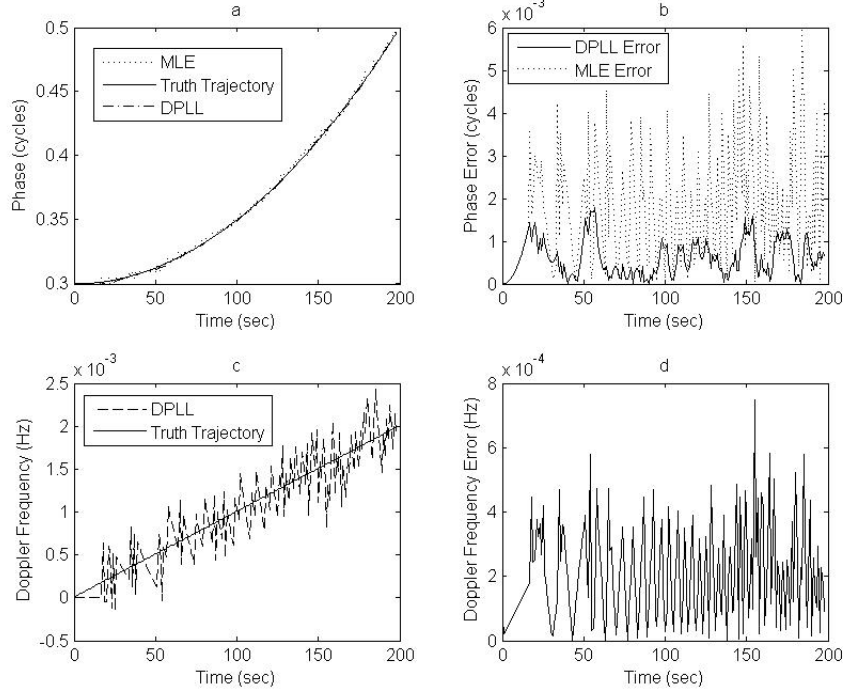


Figure 11: This figure shows the results of the simulation using the Crab Pulsar with a detector trajectory along the line-of-sight direction with an initial acceleration of 0.1 km/s^2 , zero initial velocity, and 0.3 initial phase. Plot a shows the phase over the 200 second observation. Plot b shows the phase error. Plot c contains the DPLL Doppler frequency as it tracks the desired frequency. Plot d shows the error in the DPLL frequency.

and the MLE-DPLL algorithm along with the truth trajectory. It can be seen that they both track the true phase over the observation window, but the error is smaller for the DPLL phase as expected. The phase tracks exactly one cycle out of phase, but still tracks the fractional part of the phase accurately, which is the goal. The bottom two plots show the DPLL frequency state versus the true frequency evolution and the error. The DPLL frequency is tracking with some initial fluxuations, but flattens out to a negligible amount. Figure 14 contains the results for the simulated phase tracking using the pulsar B1821-24 with a constant acceleration as given in Table 5. The top plots show the phase outputs of the MLE algorithm and the MLE-DPLL algorithm along with the truth trajectory. It can be seen that they both track the true phase over the observation window and that the error decreases down more for the DPLL phase but takes longer to settle. The bottom two plots show the DPLL frequency state versus the true frequency evolution and the error. The DPLL frequency is tracking with some fluxuations, but with an error on the order of 0.005 after an initial spike. For the case of a greater constant acceleration and nonzero initial velocity as given in Table 5, the results can be seen in Figure 15. The phase is tracking a few cycles out of phase this time, but the DPLL phase tracks the fractional part with decreasing error over the observation interval. The MLE output is growing as time progresses. It can also be seen that the Doppler frequency is being tracked well by the DPLL following an initial fluctuation of over 50 seconds.

Table 5: Descriptions of the Performed Experimental Runs

Pulsar	Type of Run	th.0	V0 (km/s)	a (km/s $\hat{2}$)	Initial f.d (hz)	Number of Runs	Observation Time (sec)
Crab	Stationary	0.5	0	0	29.9401	10	10
B1821-24	Stationary	0.5	0	0	327.4056	10	10
Crab	Constant v	0.5	1	0	29.9402	10	10
B1821-24	Constant v	0.5	1	0	327.4067	10	10
Crab	Constant a	0.3	0	0.1	29.9401	1	200
B1821-24	Constant a	0.3	0	0.1	327.4056	1	200
crab	Constant a	0.5	1	5	29.9402	1	250

Table 6: MLE Results from Experiments

Pulsar	Type of Run	Average theta_0	Error
Crab	Stationary	0.512305	2.461
B1821-24	Stationary	0.500035	0.007
Crab	Constant V	0.50816	1.632
B1821-24	Constant V	0.49387	1.226

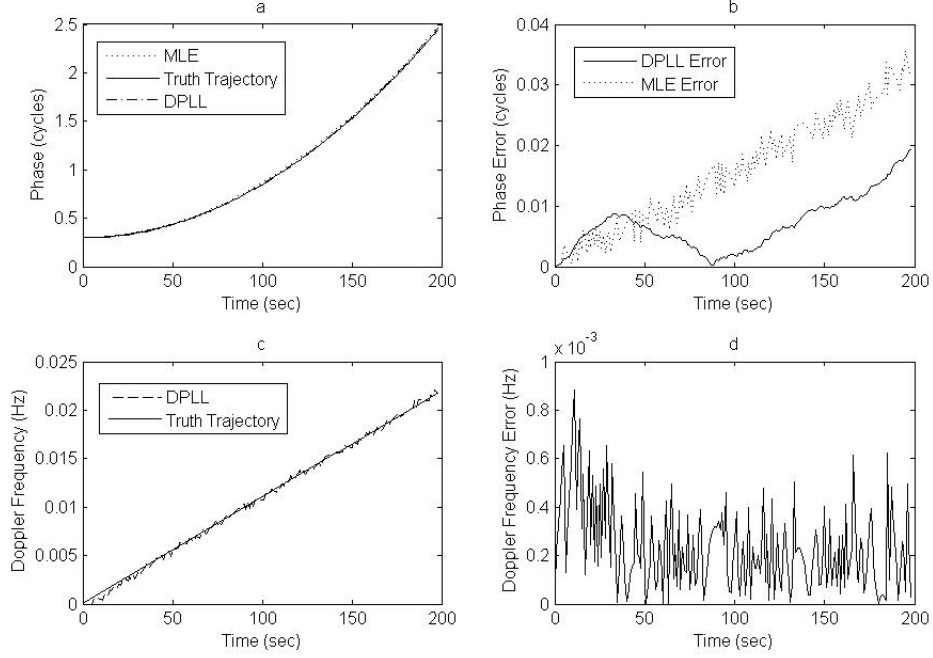


Figure 12: This figure shows the results of the experimental run using the B1821-24 pulsar with a detector trajectory along the line-of-sight direction with an initial acceleration of 0.1 km/s^2 , zero initial velocity, and 0.3 initial phase. Plot a shows the phase over the 200 second observation. Plot b shows the phase error. Plot c contains the DPLL Doppler frequency as it tracks the desired frequency. Plot d shows the error in the DPLL frequency.

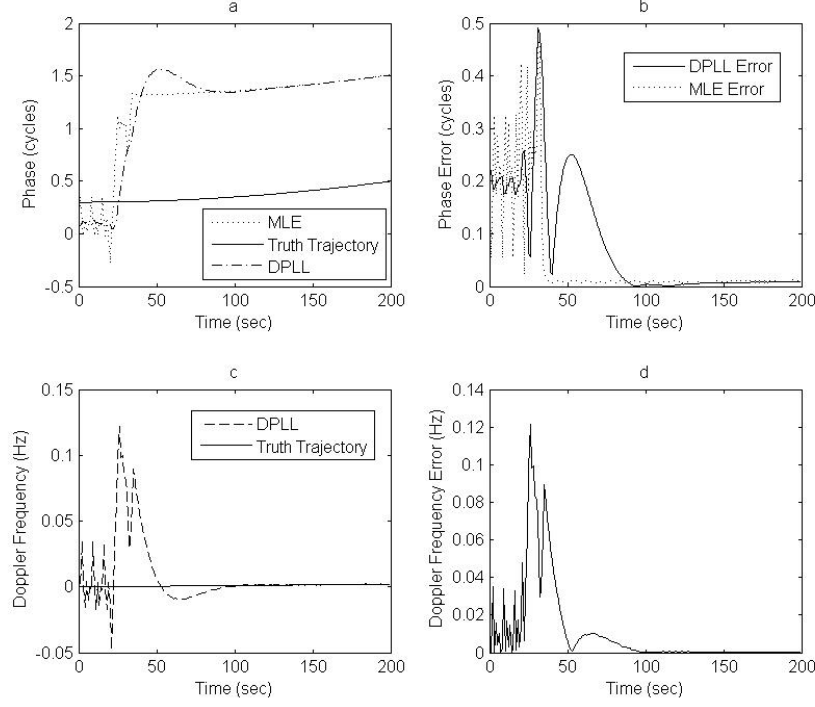


Figure 13: This figure shows the results of the experimental run using the Crab Pulsar with a detector trajectory along the line-of-sight direction with an initial acceleration of 0.1 km/s^2 , zero initial velocity, and 0.3 initial phase. Plot a shows the phase over the 200 second observation. Plot b shows the phase error. Plot c contains the DPLL Doppler frequency as it tracks the desired frequency. Plot d shows the error in the DPLL frequency.

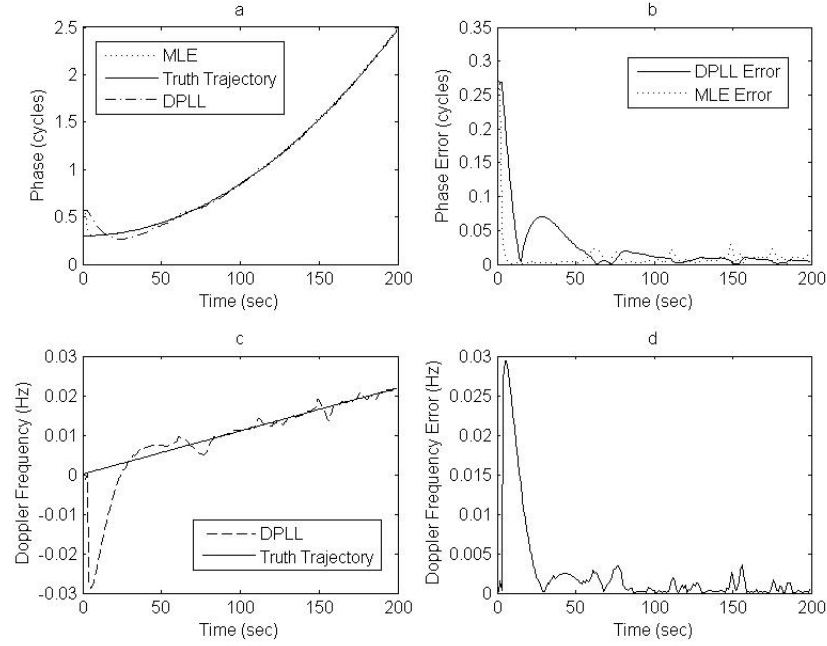


Figure 14: This figure shows the results of the experimental run using the pulsar B1821-24 with a detector trajectory along the line-of-sight direction with an initial acceleration of 0.1 km/s^2 , zero initial velocity, and 0.3 initial phase. Plot a shows the phase over the 200 second observation. Plot b shows the phase error. Plot c contains the DPLL Doppler frequency as it tracks the desired frequency. Plot d shows the error in the DPLL frequency.

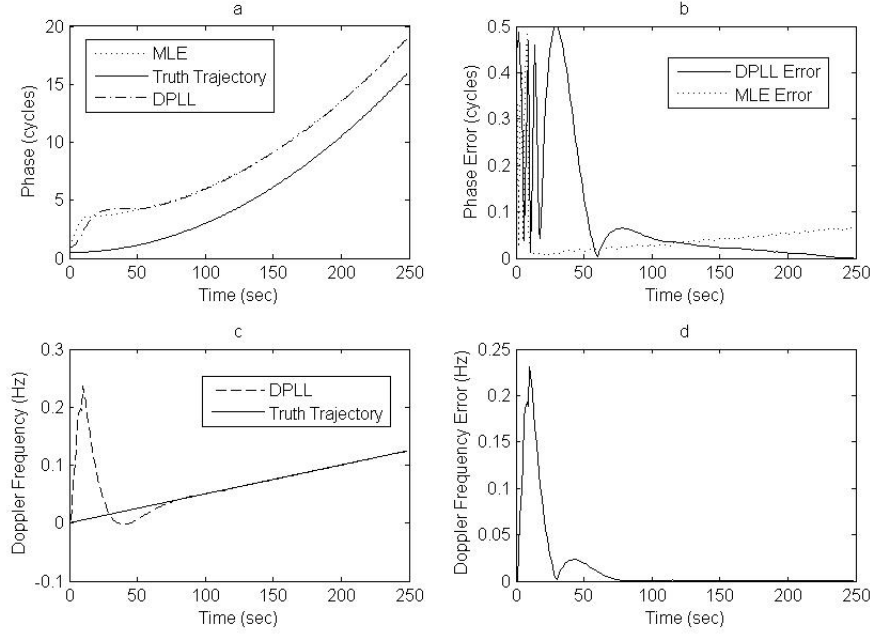


Figure 15: This figure shows the results of the experimental run using the Crab Pulsar with a detector trajectory along the line-of-sight direction with an initial acceleration of 5 km/s^2 , an initial velocity of 1 km/s , and 0.5 initial phase. Plot a shows the phase over the 250 second observation. Plot b shows the phase error. Plot c contains the DPLL Doppler frequency as it tracks the desired frequency. Plot d shows the error in the DPLL frequency.

8 Conclusion

X-ray navigation provides many opportunities for use in spacecraft applications, either as an autonomous deep space navigation system or as a means of reducing the errors as part of a larger filter also receiving DSN telemetry. Phase tracking is a method of position determination using the periodic nature of a pulsar's signal. It has the benefit of not relying on time transfer of TOAs to the SSB to compare to a template, and it allows for near continuous updates with small blocks of TOAs. In order to be implemented, though, a means of accurately estimating the phase and tracking the signal pulses is needed. For a constant frequency observed signal, an MLE is all that is required to track the phase. When the dynamical motion of the spacecraft causes the observed signal frequency to vary appreciably a cascaded MLE-DPLL algorithm was used where the observation interval was broken up into one second blocks. In this paper, these algorithms were tested for a range of scenarios with both the Crab pulsar and B1821-24. Simulated results were generated first to confirm the theory of the proposed algorithm and then experiments were run using the GXLT equipment at the GSFC. This allowed for actual X-ray photon generation using an MXS and detection using a SDD. This added complexity allowed us to test the algorithms with actual photon processing with hardware in the loop. In order to test the MLE under constant signal frequency a stationary case and a constant velocity case were considered for both pulsars. To test the MLE-DPLL cascade under the varying frequency model, a scenario with constant acceleration was considered.

In Summary, this paper has demonstrated:

- MLE was able to track the initial phase for either a stationary detector or one moving at constant velocity with error under 0.15% in each simulated case, and tracked with error under 2.5% for all of the experimental runs. Where all of these values were averaged over ten runs to offset the non-deterministic effects.
- MLE-DPLL phase tracking algorithm was validated for two experimental pulse sources for constant acceleration in one-dimension.
- MLE-DPLL was shown to accurately track the doppler frequency and the fractional component of the phase.
- MLE-DPLL tested at an acceleration of 5 km/s^2 with good results when the Crab Pulsar is the source.

In the simulations the phase and frequency were tracked for both pulsars. For the Crab pulsar the DPLL phase error was on the order of 10^{-3} and doppler frequency error was on the order of 10^{-4} . For B1821-24 the DPLL phase error grew to 0.02 cycles error in 200 seconds, which was still better than the MLE alone. The Doppler frequency was tracked with frequency error on the order of 10^{-3} . In the experimental runs the phase for the Crab pulsar tracked one cycle out of sync, but the phase error settled down to on the order of 10^{-2} . The doppler frequency also tracked after a bump over the first 50 seconds. For B1821-24 the phase tracked with error on the order of 0.05 and the doppler frequency tracked with error on the order of 0.005. An extra scenario with a higher acceleration and a nonzero initial velocity was performed experimentally with the Crab. This was to test the algorithm's durability to higher acceleration. The phase tracked with a three cycle offset with the error in the DPLL phase decreasing to 0 over 250 seconds, but the MLE phase outputs increased over the observation. The doppler phase of the DPLL tracked well after a initial transient period of approximately 75 seconds. In all cases the DPLL state estimates were better in the long run than just the MLE outputs by themselves. This shows the utility of adding the DPLL in the loop in order to decrease the phase error and produce an estimate of the doppler frequency. The results experimentally validated the phase-tracking algorithm using lab equipment in place of an actual pulsar and one dimensional trajectories. Future work includes looking into methods of speeding up the MLE search algorithm including using fourier transforms on the incoming data. Also, DPLLs of higher order will be considered in order to see if they can better deal with the effects of nonzero acceleration in some of the test cases. Three dimensional orbits will be another logical experimental extension of this work. Overall, the pulse phase tracking algorithm achieved experimental results matching up with the simulated functionality of the algorithm and it would be ideal for use in an XNAV system.

Acknowledgements

I would like to thank the Neutron-star Interior Composition Explorer (NICER) and Station Explorer for X-ray Timing and Navigation Technology (SEXTANT) teams at the NASA Goddard Space Flight Center (GSFC) for allowing me to work with them, use their laboratory testbed setup, and for all of their help and support. In particular, Dr. Keith Gendreau, Dr. Jason Mitchell, Dr. Munther Hassouneh, and Dr. Luke Winternitz for their help in understanding and learning how to run the equipment. Additionally, I would like to thank Dr. Suneel Sheikh of ASTER Labs, Inc., Dr. John Hanson of CrossTrac Engineering, and Patrick Doyle and Dr. Demoz Gebre-Egziabher of the University of Minnesota for their help with developing algorithms for photon generation and incorporating doppler effects and time delays for the simulations.

References

- [1] Golshan, A. R. and Sheikh, S. I., "On Pulse Phase Estimation and Tracking of Variable Celestial X-Ray Sources," *Proceedings of the 63rd Annual Meeting of the Institute of Navigation*, Cambridge, MA, April 2007, pp. 413-422
- [2] Samus, N. N., and Durlevich, O. V., "General Catalogue of Variable Stars (GCVS) Variability Types and Distribution Statistics of Designated Variable Stars According to their Types of Variability," [online database], URL: <http://www.sai.msu.su/groups/cluster/gcvs/gcvs/iii/vartype.txt>.
- [3] Hewish, A., Bell, S. J., Pilkington, J. D., Scott, P. F., and Collins, R. A., "Observation of a Rapidly Pulsating Radio Source," *Nature*, Vol. 217, 1968, pp. 709-713.
- [4] Lyne, A. and Graham-Smith, F., *Pulsar Astronomy*, Third Edition, Cambridge University Press, Cambridge UK, 2005.
- [5] Manchester, R. N. and Taylor, J. H. *Pulsars*, W. H. Freeman and Company, San Francisco, 1977.
- [6] Baade, W. and Zwicky, F., "On Super-Novae," *Proceedings of the National Academy of Science*, Vol. 20, No. 5, 1934, pp. 254-259.
- [7] Oppenheimer, J. R. and Volkoff, G. M., "On Massive Neutron Cores," *Physical Review*, Vol. 55, 1939, pp. 374-381.
- [8] Sheikh, S. I., Hanson, J. E., Graven, P. H., and Pines, D. J., "Spacecraft Navigation and Timing Using X-ray Pulsars," *Navigation: Journal of The Institute of Navigation* Vol. 58, No. 2, Summer 2011.
- [9] Kaspi, V. M., Taylor, J. H., and Ryba, M. F., "High-Precision Timing of Millisecond Pulsars. III: Long-Term Monitoring of PSRs B1855+09 and B1937+21," *Astrophysical Journal*, Vol. 428, 1994.
- [10] Matsakis, D. N., Taylor, J. H. and Eubanks, T. M., "A Statistic for Describing Pulsar and Clock Stabilities," *Astronomy and Astrophysics*, Vol. 326, 1997, pp. 924-928.
- [11] Thornton, C. L., and Border, J. S., *Radiometric Tracking Techniques for Deep Space Navigation*, John Wiley and Sons, Hoboken, NJ, 2003.
- [12] Gounley, R., White, R., and Gai, E., "Autonomous Satellite Navigation by Stellar Refraction," *Journal of Guidance, Control, and Dynamics*, Vol. 7, No. 2, 1984, pp. 129-134.
- [13] Lanyi, G., Bagri, D. S., and Border, J. S., "Angular Position Determination by Spacecraft by Radio Interferometry," *Proceedings of the IEEE*, November 2007.
- [14] Buist, P. J., Engelen, S., Noroozi, A., Sundaramoorthy, P., Verhagen, S., and Verhoeven, C., "Overview of Pulsar Navigation: Past, Present and Future Trends" *Navigation: Journal of The Institute of Navigation* Vol. 58, No. 2, Summer 2011.
- [15] RXTE Science Operations Facility, "XTE ASM Catalog," [online], URL: <http://rxte.gsfc.nasa.gov/docs/xte/SOF/ASMCatalog.html>
- [16] Gendreau, K. C., Arzoumanian, Z., Okajima, T., and the NICER Team, "The Neutron-star Interior Composition Explorer (NICER): an Explorer mission of opportunity for soft X-ray timing spectroscopy," *Proceedings of SPIE in Space Telescopes and Instrumentation: Ultraviolet to Gamma Ray*, volume 8443, September 2012.
- [17] Winternitz, L. M., Hassouneh, M. A., Gaeber, J. A., Mitchell, J. W., Gavril, F., Arzoumanian, Z., and Gendreau, K. C., "An X-Ray Navigation Ground Testbed," *27th Space Sim Conference*, Annapolis, MD, November 2012.
- [18] NASA/CXC/ASU/J. Hester et al., "Crab Nebula Composite Image," [online], URL: <http://chandra.harvard.edu/photo/2002/0052/more.html>
- [19] Downs, G. S., "Interplanetary Navigation Using Pulsating Radio Sources," *NASA Technical Reports N74-34150*, 1974, pp. 1-12.
- [20] Hanson, J. E., *Principles of X-Ray Navigation*, Ph.D. Thesis, Stanford University, 1996, URL: <http://il.proquest.com/products/umi/dissertations/>.

- [21] Sheikh, S. I., *The Use of Variable Celestial X-ray Sources for Spacecraft Navigation*, Ph.D. Thesis, University of Maryland, 2005, URL: <https://drum.umd.edu/dspace/handle/1903/2856>.
- [22] Sheikh, S. I., Golshan, A. R., and Pines, D. J., "Absolute and Relative Position Determination Using Variable Celestial X-Ray Sources," *30th Annual AAS Guidance and Control Conference*, American Astronautical Society, Breckenridge, CO, 3-7 February 2007.
- [23] Sheikh, S. I. and Pines, D. J. "Recursive Estimation of Spacecraft Position and Velocity Using X-Ray Pulsar Time of Arrival Measurements," *Navigation*, Vol. 53, No. 3, Fall 2006, pp. 149-166.
- [24] Sheikh, S. I., Pines, D. J., Wood, K. S., Ray, P. S., Lovellette, M. N., and Wolff, M. T., "Spacecraft Navigation Using X-ray Pulsars," *Journal of Guidance, Control, and Dynamics*, Vol. 29, No. 1, 2006.
- [25] Sala, J., Urruela, A., Villares, X., Estalella, R., and Paredes, J. M., "Feasibility Study for a Spacecraft Navigation System relying on Pulsar Timing Information," *European Space Agency Advanced Concepts Team ARIADNA Study*, 03/4202, 23 June 2004.
- [26] Wallace, K., "Radio Stars, What They Are and The Prospects for their Use in Navigational Systems," *Journal of Navigation*, Vol. 41, No. 3, 1988, pp. 358-374.
- [27] Chester, T. J., and Butman, S. A., "Navigation Using X-ray Pulsar," *NASA Technical Reports N81-27129*, 1981, pp. 22-25.
- [28] Durrett, R., *Essentials of Stochastic Processes*, Springer, New York, 1999.
- [29] Bar-David, I., "Communication under the Poisson Regime" *IEEE Transactions on Information Theory*, Vol. 15, No. 1, January 1969, pp. 31-37.
- [30] Eliason, S. R., *Maximum Likelihood Estimation Logic and Practice*, Sage Publications, Newbury Park, California, 1993.
- [31] Shenton, L. R. and Bowman, K. O., *Maximum Likelihood Estimation in Small Samples*, Macmillan Publishing Co., Inc., New York, 1997.
- [32] Rinauro, S., Colonnese, S., and Scarano, G., "Fast near-maximum likelihood phase estimation of X-ray pulsars," *Signal Processing* Vol. 93, 2013, pp. 326-331.
- [33] Al-Araji, S. R., Hussain, Z. M., and Al-Qutayri, M. A., *Digital Phase Lock Loops: Architectures and Applications*, Springer, Dordrecht, The Netherlands, 2006.
- [34] Lindsey, W. C. and Chie, C. M., "A Survey of Digital Phase-Locked Loops", *Proceedings of The IEEE*, Vol. 69, No. 4, April 1981.
- [35] Thomas, J. B., "An Analysis of Digital Phase-Locked Loops," *NASA JPL Publication 89-2*, February 1989.
- [36] Best, R. E., *Phase-Locked Loops: Design, Simulation, and Applications*, Fifth Edition, McGraw-Hill, New York, 2003.
- [37] Egan, W. F., *Phase-Lock Basics*, Second Edition, IEEE, New York, 2008.
- [38] Stephens, S. A. and Thomas, J. B., "Controlled-Root Formulation for Digital Phase-Locked Loops," *IEEE Transactions on Aerospace and Electronic Systems*, Vol. 31, No. 1, January 1995.
- [39] Devroye, L., *Non-Uniform Random Variate Generation*, Chapter VI, Springer-Verlag, 1986, [online book], URL: <http://luc.devroye.org/rnbookindex.html> [cited March 15, 2012].
- [40] Emadzadeh, A. A. and Speyer, J. *Navigation in Space by X-ray Pulsars*, Springer, New York, 2011.
- [41] Sheikh, S. I., Hellings, R. W., and Matzner, R. A., "High-Order Pulsar Timing For Navigation," *Proceedings of the 63rd Annual Meeting of The Institute of Navigation*, Cambridge, MA, April 2007, pp. 432-443.
- [42] Gendreau, K., Arzoumanian, Z., Koenecke, R., and Deines-Jones, P., "A Modulated X-ray Source for In-flight calibration of High-Energy Astrophysics Instrumentation," *SPIE Proceedings* 8443 (2012).
- [43] Prigozhin, G., Gendreau, K., Foster, R., Ricker, G., Villasenor, J., Doty, J., Kenyon, S., Arzoumanian, Z., Redus, R., and Huber, A., "Characterization of the Silicon Drift Detector for NICER Instrument," *SPIE Proceedings*, 8453, Part 1, 2012.